Journal of
Materials Chemistry C

ROYAL SOCIETY
OF CHEMISTRY

PAPER

View Article Online
View Journal

Check for updates

Cite this: DOI: 10.1039/d5tc03384e

Intrinsic piezoresistive mechanism of conductive porous nano-composites with linearity assumption: theoretical and experimental analyses

Yu Duan, Hua An, Weigao Wang, Chao Shang, Jianpeng Zhang* and Zhengchun Peng*

Porous piezoresistive nanocomposites (PPNs) are pivotal for the development of advanced flexible sensors due to their unique combination of compressibility, low density, and breathability. However, their rational design is hindered by a fundamental disconnect: existing models either treat mechanical deformation (*e.g.*, pore collapse) and electrical conduction (*e.g.*, tunneling) in isolation or rely on empirical parameters, lacking clear physical links to the microstructure. This gap obscures the intrinsic piezoresistive mechanism, particularly the dominant role of ligament bending (rather than pore closure) in governing resistance changes under small-to-moderate strains. Herein, we propose a theoretical model that directly couples the micromechanics of porous structures with the evolution of their conductive network. By integrating the Timoshenko beam theory (for ligament bending/stretching) with quantum tunneling theory within a periodic Gibson-Ashby unit cell, our model quantifies piezoresistive response through key microstructural and electrical parameters. The experimental validation of the proposed model was conducted by measuring the piezoresistive behaviors of different types of PPNs. Furthermore, we extend this framework by incorporating viscoelasticity (Kelvin–Voigt model) to accurately capture time-dependent relaxation behaviors—a critical feature for dynamic sensing. Transcending phenomenological fitting, this work provides a predictive and generalizable toolset for the physics-guided, microstructure-informed design of high-performance PPN sensors.

Received 11th September 2025,
Accepted 17th March 2026

DOI: 10.1039/d5tc03384e

rsc.li/materials-c

1. Introduction

The burgeoning field of flexible electronics, encompassing applications such as biomedical engineering,[1,2] health monitoring,[3,4] wearable devices,[5,6] and soft robotics,[7] has spurred an urgent demand for sensing materials that are simultaneously highly sensitive, mechanically compliant, and biocompatible. Porous piezoresistive nanocomposites (PPNs), formed by embedding conductive nanofillers within a deformable porous polymer matrix, have emerged as a leading candidate.[8] Their three-dimensional (3D) interconnected porous architecture endows them with exceptional flexibility, ultra-low density, high compressibility, and inherent breathability—properties indispensable for long-term, conformable biological interfacing.[4,9,10] Consequently, PPNs are regarded as an ideal platform for developing next-generation flexible pressure and strain sensors.[11]

However, the rational design of PPNs with tailored performance hinges on a fundamental understanding of the intricate relationship between their microstructural evolution under load and the resultant macroscopic electromechanical response. This necessitates the development of robust theoretical models capable of accurately predicting and elucidating their piezoresistive behaviors. Substantial efforts have been devoted to modeling the structure–property relationships of porous materials.[12] For mechanical properties, models such as the Gibson-Ashby (GA) theory,[12–15] which simplifies structures into cubic pores,[13] and polyhedron-based models (*e.g.*, Kelvin,[16] Octahedral,[12] and rhombic dodecahedron)[17] have been widely used. The GA model accurately analyzes the mechanical properties,[14,15] such as tensile and compressible behaviors, of porous composites but struggles with determining other physical properties.[12,18] The Kelvin model, which employs space-filling Kelvin cells and assumes Plateau border cross-sections with variable areas for ligaments,[16] closely resembles the actual foams but requires more parameters than the GA model to determine mechanical and thermal properties.[12] To enhance accuracy, simulation strategies combining Voronoi tessellation and Monte Carlo methods with

---

Center for Stretchable Electronics and Nano Sensors, Key Laboratory of Optoelectronic Devices and Systems of Ministry of Education, College of Physics and Optoelectronic Engineering, Shenzhen University, Shenzhen 518060, China. E-mail: zhangjp@szu.edu.cn, zcpeng@szu.edu.cn

these models have been developed using the finite element method (FEM) to obtain detailed attribute characteristics of porous structures.[18–20] For electrical and thermal transport, conduction is often described through pathways comprising solid conduction, gaseous conduction, and their coupling within the porous network.[21] Other specialized models have been proposed to study specific properties of porous materials, such as electrical resistance,[11] acoustic features,[22] surface area characteristics,[23,24] piezoelectric response,[15] permeability,[25] and electromagnetic shielding.[26] In these models, nonlinearity in the mechanical response of open-cell foams is often governed by the buckling of cell ligaments[13,16] In piezoelectric foams, the strain-gradient-induced polarization arises from complex deformations, such as beam bending,[15] pyramid compression,[27] cylinder twisting,[28] or atomic-scale crack excitation.[29] The above research demonstrates that using various mechanics-based single-cell analysis models can accurately study the properties and performance characteristics of porous materials.

By employing characteristic models, such as diamond structures[30] and cross structures,[31,32] accompanied by corresponding equivalent circuit models, research on the piezoresistive properties of porous materials has been able to unveil the exceptional sensitivity of porous materials to localized pore closure during compression, thereby contributing significantly to their distinct piezoresistive behavior. In the realm of flexible substrates incorporating nano-conductive particles, the application of theories, such as tunneling theory,[33] percolation theory,[34] and contact theory,[31] allows for an analysis of how variations in inter-particle gaps impact the resistivity of the material. These well-established theories and models deepen our comprehension of electron transport phenomena in porous materials and provide insights into their influence on the piezoresistive response. Particularly, the tunneling effect assumes a crucial role in explaining the low percolation threshold and non-linear electrical behavior observed in solid piezoresistive nanocomposites (SPNs).[35] A comprehensive theoretical model grounded in tunneling theory and utilizing only two adjustable parameters has been developed, accurately capturing the relative variation in resistance under applied strain.[36] The inherently high porosity of porous materials imparts them with enhanced compressibility, making pore closure a primary factor contributing to the observed piezoresistive characteristics. Micropore closure is modeled as a function of porosity using these two adjustable parameters, which can be further refined through precise fitting to actual experimental data.[37]

However, a significant gap exists when applying these models to predict the piezoresistive behavior of PPNs. Traditional approaches often treat mechanical deformation (*e.g.*, pore closure or ligament bending) and electrical conduction (*e.g.*, percolation and tunneling) in isolation. For instance, while characteristic models coupled with equivalent circuits can highlight sensitivity from pore closure,[37] they often rely on empirical parameters with obscure physical meanings. Conversely, theories such as the tunneling theory effectively describe electron transport in composites but typically do not explicitly couple with the specific, microstructure-dependent mechanical deformation of a porous matrix.[35,36] Prominent structural models, such as the GA cell, Kelvin cell, and Octahedral cell, renowned for their precision in stress response analysis, tend to possess inadequate capabilities in capturing the pore closure phenomenon under conditions characterized by small deformations. This disconnect results in models that are either purely phenomenological or limited to specific deformation regimes. The piezoresistive response of porous conductive nanocomposites is known to involve two main mechanisms: changes in the conductive network within the solid matrix[35] and the closure of micropores.[37] While tunneling effects are recognized as the key to explaining the low percolation threshold and nonlinear behavior in solid composites,[35] and micropore closure has been modeled as a function of porosity,[37] a unified framework linking these electrical mechanisms to the micromechanics of porous deformation is lacking. Particularly, the prevalent assumption that pore closure is the primary source of piezo-resistance may overlook the potentially dominant role of tunneling effects arising from pore wall (ligament) bending with small-to-moderate compressive deformations.[38,39] This lack of a unified, physics-based model that directly couples micromechanics with charge transport has hindered the accurate prediction and optimization of PPNs' performance, especially their high intrinsic sensitivity observed under small strains.[40–42]

We present a novel analytical model that explicitly couples the micromechanical deformation of the porous structure with the evolution of its electrical conduction network to predict the piezoresistive behavior of PPNs. Departing from models that prioritize pore closure, we posit that for open-cell PPNs under small-to-moderate compressions, the bending of cell ligaments—rather than full pore closure—is a dominant deformation mode, and the consequent variation in tunneling gaps between the conductive fillers embedded in these ligaments governs the primary piezoresistive response. This model integrates the Timoshenko beam theory[40,41] to describe the bending of idealized ligaments and couples it with the quantum tunneling theory to calculate the inter-particle resistance change. It allows for the systematic evaluation of key design parameters including porosity, conductive filler loading, pore geometry, and the effective matrix constraint within the polymer network (quantified by the factor ξ). To experimentally validate the model, we fabricate carbon black/thermoplastic polyurethane (CB/TPU) PPNs with varied compositions. Their intrinsic piezoresistive response is meticulously characterized using a four-wire measurement method, while SEM imaging provides critical inputs for microstructural parameters. Furthermore, recognizing the viscoelastic nature of the polymer matrix, we extend our framework by incorporating a Kelvin–Voigt model[43–45] to accurately capture the time-dependent piezoresistive relaxation and creep behaviors, which are crucial for dynamic sensing applications. This combined theoretical–experimental approach yields a physics-informed model capable of not only fitting experimental data with high accuracy but also providing deep insights into the underlying mechanisms, guiding the design of PPNs for high-sensitivity, lightweight wearable electronics and biomimetic tactile sensing systems.[46]

2. Piezoresistive model and mechanism of PPN

PPNs are a class of materials where conductive nano-fillers are uniformly dispersed within the cell ligaments of a polymer matrix. Fig. 1a and b illustrate scanning electron microscopy (SEM) images, showcasing the open-cell structure of a typical PPN and the cell ligament with homogeneous carbon black (CB) fillers, respectively. To interpret the piezoresistive behavior of PPNs, a periodic structure based on the Gibson-Ashby (GA) unit cell, as depicted in Fig. 1d, along with a representative GA cell shown in Fig. 1e, is utilized. This simplification captured the essential deformation mechanics of open-cell foams while remaining analytically tractable. Furthermore, an equivalent circuit model was proposed within the GA cell (Fig. 1f) to examine the electrical bulk resistance in relation to deformation, taking into account both the tunneling effect theory and beam theory.

The model was built upon the following key assumptions. (1) Small-strain, linear elastic material behavior: the model is valid for compressive strains ($\varepsilon < 50\%$), where the mechanical response of the polymer matrix and the structural deformation of the GA cell remain approximately linear-elastic and reversible. (2) Ligament bending as the dominant deformation mode: the primary mechanical response is the bending of cell ligaments, modeled as Timoshenko beams. This assumes no large-scale pore collapse, ligament buckling, or plastic yielding. (3) Homogeneous and isotropic microstructure: the conductive filler (CB) is uniformly distributed, and the porous structure is represented by a periodic, isotropic Gibson-Ashby unit cell. (4) Tunneling-dominated conduction: electrical conduction is governed by quantum tunneling between adjacent filler particles, described by an exponential distance dependence.[35,36]

In order to establish a quantitative understanding of the relationship between electrical bulk resistance and deformation, an analytical piezoresistive model was developed. This model incorporated considerations of the aforementioned theories and provided insights into the underlying mechanisms governing the piezoresistive response of PPNs. The findings of this study have implications for various applications, ranging from sensing devices to smart materials. Understanding the intricate interplay between the structural characteristics of PPNs and their corresponding electrical properties opens up opportunities for the design and optimization of novel piezoresistive materials with enhanced performance and functionality.

2.1. Geometric structure and equivalent circuit model

Based on the principles of physics and deformation mechanisms underlying open-cell foam structures, a Gibson–Ashby (GA) unit cell model was employed in this study to investigate the mechanical properties of such foams. The GA model considered a cubic arrangement of members within the foam

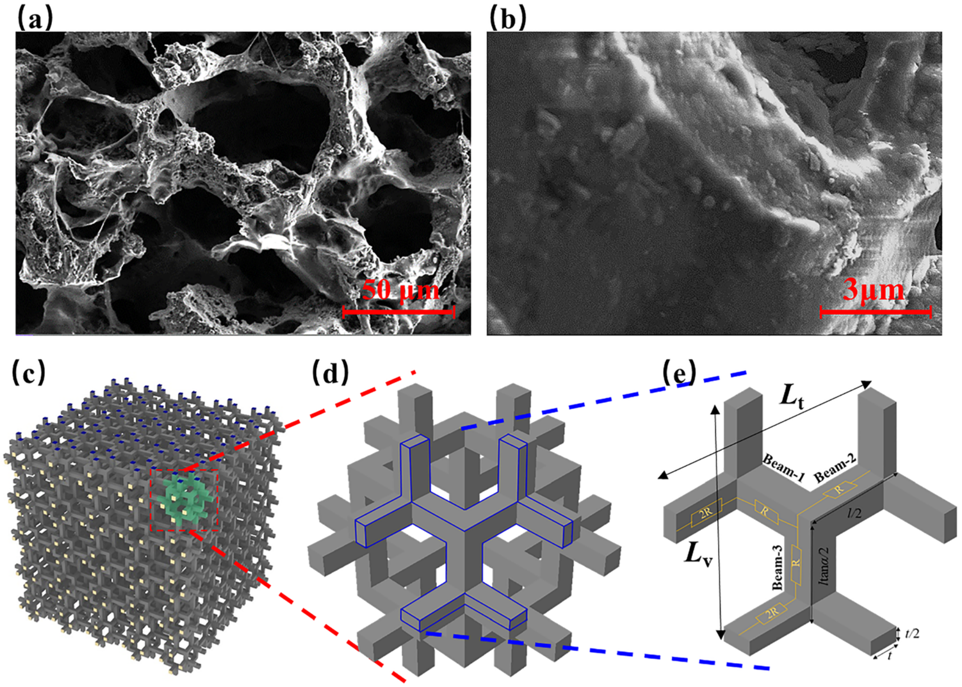

Fig. 1 Porous cell structure of PPN and its simplified model. SEM images of the cell structure (a) and cell ligament with conductive fillers (b). Three-dimensional (3D) theoretical models of the PPN, including GA periodic structures (c), a GA cell (d) and an equivalent circuit model (e).

structure (as depicted in Fig. 1c). Previous research efforts[13,15] have utilized this model to analyze various characteristics of PPNs, extending beyond their mechanical performance to include phenomena such as the flexoelectric effect. In the present investigation, the focus was directed towards examining the electrical conductivity of PPNs using the GA model. The objective was to gain a comprehensive understanding of the piezoresistive behavior exhibited by these materials. Specifically, for the GA cell represented in Fig. 1d, the relative density (p) is defined as the ratio between the density of the porous material and the density of its solid matrix, which is given by:

$$p = \frac{[(2\tan\alpha + 1) - 5\theta]\theta^2}{(\tan\alpha - \theta)^2(1-\theta)}, \tag{1}$$

where $\tan\alpha = \frac{L_v}{L_t}$ is the structural parameter of the GA cell, which is defined as the relative value of the length of a vertical beam against *vs.* that of a transverse beam, and $\theta = \frac{t}{l}$ is the width-length ratio of a simplified beam model with a square cross-section. The internal matrix of porous materials contains a significant amount of nanoscale conductive materials, which are uniformly distributed through prolonged mixing and blending. As a result, the electrical conductivity distribution on the pore wall beam units is approximately uniform and consistent. Therefore, the electrical conducting model was modified with respect to the model given in Fig. 1e. Thus, the total equivalent resistance yields

$$R_\mathrm{c} = \frac{(2R_\mathrm{B} + R_\text{beam-1})(2R_\mathrm{B} + R_\text{beam-3})}{4R_\mathrm{B} + R_\text{beam-1} + R_\text{beam-3}} + R_\text{beam-2}, \tag{2}$$

where $R_\text{beam-1}$, $R_\text{beam-2}$ and $R_\text{beam-3}$ are the resistance of beam-1, beam-2 and beam-3, which undergo significant deformation. R_B represents the resistance of beams that primarily carry electrical circuit transmission without undergoing significant deformation.

2.2. Piezoresistive model of a cell ligament containing conductive fillers

As per the proposal by Ezquerra *et al.*,[40] a straightforward model based on the tunneling theory has been introduced to describe the correlation between the resistivity of a conductive nanocomposite and the concentration of conductive fillers, as well as the inter-particle distance. The model is mathematically represented as follows:

$$\rho = \rho_0 \mathrm{e}^{2Xd}, \tag{3}$$

where $X = \frac{\sqrt{2mV(T)}}{h}$, ρ_0 is the resistivity of the conductive fillers, m is the mass of the charge carriers, $V(T)$ is the temperature-modified barrier height, and d is the distance between conductive particles, which is approximately proportional to $\phi^{\frac{-1}{3}}$ (ϕ is the volume fraction of the conductive fillers). The earlier researchers successfully utilized the model to accurately predict the variation curve of electrical resistance in conductive composites with changes in the content of conductive carbon black, carbon nanotubes, and other components.[47] The presence of pore structure in porous materials modifies their electrical conductivity properties. Numerous studies have proposed models for the variation in the conductivity of materials with changes in the pore structure, assuming a regular geometric structure.[21] However, during the formation process of porous materials, as per the Flory–Huggins solution theory,[48] an interfacial tension between the porogen and macromolecular solution leads to the development of a macromolecular chain along the axial direction of the pore wall (Fig. 2a). Upon the evaporation of the organic solvent, microcellular structures are generated, filling the voids left by the solvent (Fig. 2b). Subsequently, a porous structure forms with a macromolecular chain aligned along the axis of the pore wall (Fig. 2c). Furthermore, the nanoscale conductive particles are uniformly distributed within the pore walls through adsorption or filling mechanisms (Fig. 2d), forming a homogeneous conductive network. Thus, the initial spacing between conductive particles is dependent on the relative density, as expressed by:

$$d_0 = np^{-c}\phi_\mathrm{c}^{-\frac{1}{3}}, \tag{4}$$

where n is the proportionality coefficient, c is the index of correlation, and ϕ_c is the volume fraction of conductive fillers against the matrix. When the cell ligament undergoes compression, a bending beam structure is formed, as depicted in Fig. 2e. Additionally, a deformed element resulting from the bending beam can be observed in Fig. 2f. The distance between conductive fillers during the deformation of the cell ligaments can be estimated using the following equation:

$$d \approx d_0\left[1 + \varepsilon + \frac{\gamma^2}{2}\right], \tag{5}$$

where ε and γ are normal strain and shear strain, respectively. In the deformed element, the normal strain results in a change in bond angle and bond length (Fig. 2g). The generation of these beam unit models primarily originates from the gaps between the pore-forming agents. Simultaneously, the interfacial tension between the pore-forming agents and the porous slurry substrate causes the polymer chains to distribute along the long axis of the beams. During the compression process of porous materials, the shear deformation in the pore wall structures induces stretching deformation in the conductive network (Fig. 2h and i) and segmental motion (Fig. 2j). This stretching leads to an increased spacing between conductive particles, resulting in elevated resistance. Additionally, the presence of dispersed macromolecular chains along the axis of the pore wall causes segmental motions when subjected to shear strain. These segmental motions disrupt the conductive paths, further contributing to an increase in the resistance of the cell ligament.[49] Therefore, in our analytical model, we introduce an analytical variable ($\xi \in (0,1]$) to investigate this phenomenon. Parameter ξ is introduced as a constraint efficacy factor, which phenomenologically

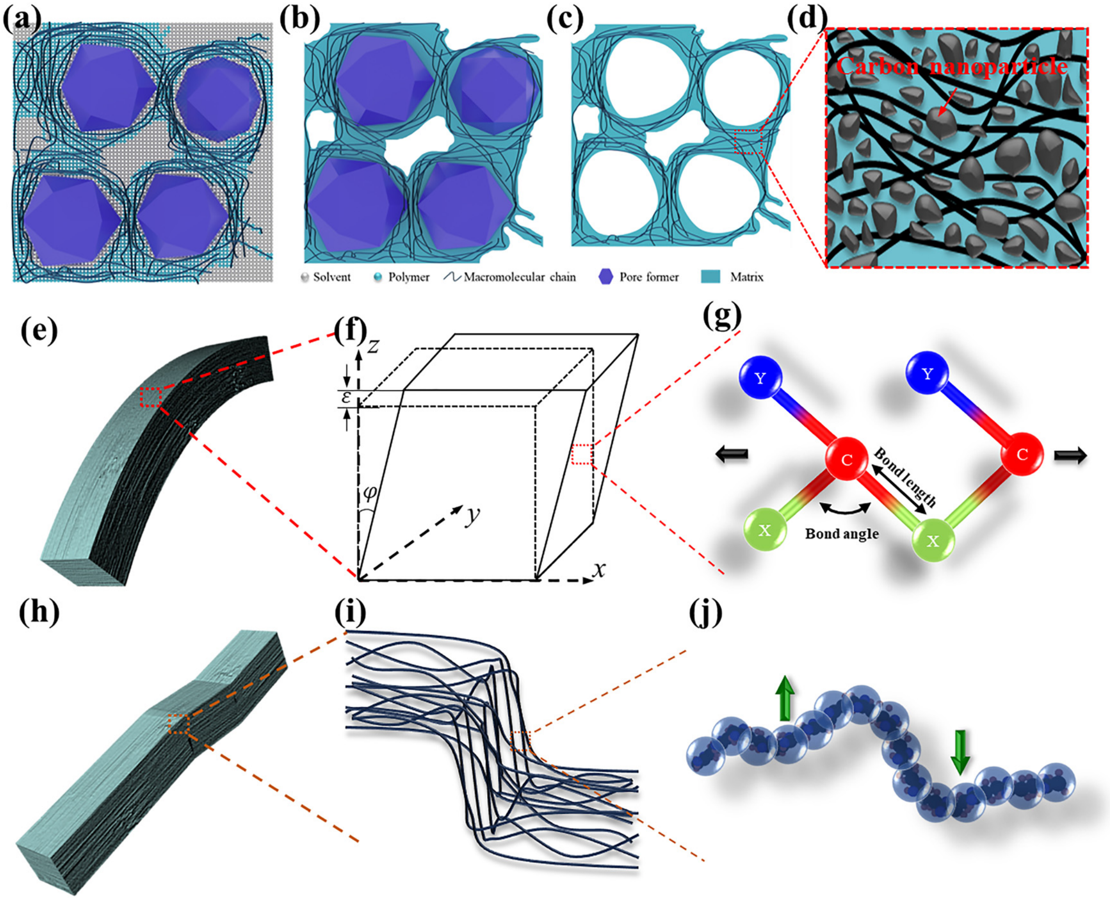

Fig. 2 Forming process and distribution at the pore wall of macromolecular chains. (a) Flory–Huggins macromolecular solution model. (b) Schematic of the porous precursor after evaporating the organic solvent. (c) Porous structure and the distribution of the macromolecular chains. (d) Schematic of the local magnification of a conductive composite material containing carbon black nanoparticles. (e) Bending beam model containing macromolecular chains. (f) Local compression deformation beam element. (g) Changes in bond angle and bond length. (h) Shear beam model containing macromolecular chains. (i) Local shear deformation of macromolecular chains. (j) Segmental motion of the macromolecular chain.

quantifies how effectively the polymer matrix constrains filler movement and chain slippage under shear deformation. A high ξ indicates a significantly constrained network. Note, $\xi = 1$ is defined as the reference state within our model for compressive strains $\leq 50\%$, where the shear-induced resistance change is solely attributed to the affine geometric deformation of the network. Phenomenologically, this corresponds to a condition where the constraint against shear-induced chain slippage is sufficiently effective that its additional contribution to resistance is negligible within our experimental detection framework. We conceptually associate this state with a highly constrained or effectively crosslinked network under the defined deformation conditions. The alteration in the distance between conductive fillers can be expressed as follows:

$$\delta = 1 + \varepsilon + \frac{\gamma^2}{2\xi}. \tag{6}$$

The resistivity of PPNs changing with deformation is expressed as

$$\rho = \rho_0 \mathrm{e}^{2Xnp^{-c}\phi_c^{-\frac{1}{3}}\left[1+\varepsilon+\frac{\gamma^2}{2\xi}\right]}. \tag{7}$$

When composites with conductive fillers are compressed to a specific strain, the change in electrical resistance can be predicted by confirming three unknown parameters, Xn, c and ξ.

2.3. Piezoresistive beam model for PPNs

Due to the presence of structural symmetry in GA units, the deformation of surrounding units during compression is uniformly identical. Therefore, employing a simplified two-dimensional structure with symmetrical analysis along one direction (with uniform thickness distribution), the overall deformation characteristics of the three-dimensional model can be effectively analyzed (Fig. 3). In the analysis of deformation in GA unit structures using beam models, it has been observed that the aspect ratio of ligaments in most porous materials is typically less than 10. Wang *et al.*[50] conducted research on the differences between the Euler and Timoshenko beam models and concluded that the Timoshenko model provided more accurate predictions of beam deformation. Furthermore, Zhang *et al.*[15] utilized a coupling approach combining the Timoshenko model and GA units to analyze the

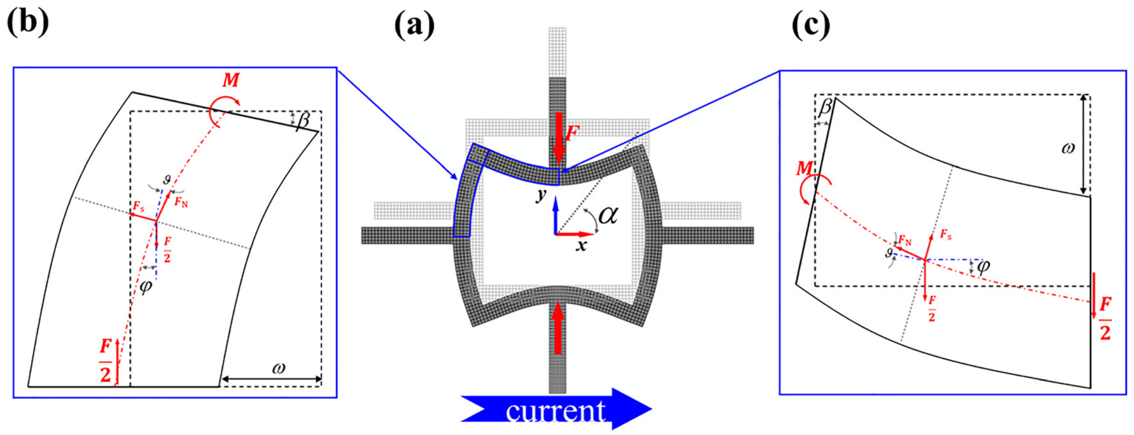

Fig. 3 Timoshenko beam model within the key deformed element of the GA model. (a) Deformed element of the GA model. (b) Vertical Timoshenko beam model against the direction of the current. (c) Transverse Timoshenko beam model against the direction of the current.

flexoelectric effect of porous materials. Hence, in our study, the combination of the GA models and Timoshenko beam models was employed to analyze the piezoresistive effect of porous materials, considering the compression resistance, resulting in accurate outcomes. The governing equation of the beam is given by

$$EI\varphi'' + \kappa GA(w' - \varphi) = 0, \tag{8}$$

where $\kappa = \frac{10(1+\mu)}{(12+11\mu)}$ is the shear correction factor for a beam with a square cross-section, whereupon the relation between the shear area (A_s) and the actual cross-sectional area (A) is employed. Fig. 3 shows the key deformed element in the GA model. The boundary condition for the transverse beam and vertical beam was determined by achieving a balance between force equilibrium and deformation compatibility, as:

$$\begin{cases} w_T|_{x=-\frac{l\tan\alpha}{2}} = 0 \\ \varphi_T|_{x=-\frac{l\tan\alpha}{2}} = \beta_0 \\ \varphi_T|_{x=0} = 0 \\ M_T|_{x\le 0} = -M + \frac{F}{2}\left(x + \frac{l\tan\alpha}{2}\right) \end{cases} \text{and} \begin{cases} w_V|_{y=0} = 0 \\ \varphi_V|_{y=\frac{l}{2}} = -\beta_0 \\ \varphi_V|_{y=0} = 0 \\ M_V|_{0\le y\le\frac{l}{2}} = M \end{cases}, \tag{9}$$

where w denotes the beam deflection, φ is the sectional angle of the Timoshenko beam, and M is the support reaction moment at the junction of the transverse beam and the vertical beam. By applying appropriate force and moment balance boundary conditions at the junctions of the beams (see Appendix A.1 for detailed derivation), we solved for the beam deflections (M_0) and rotations (β_0):

$$\begin{cases} M = \frac{\tan\alpha^2 Fl}{8(1+\tan\alpha)} \\ \beta_0 = \frac{Fl^2\tan\alpha}{16(1+\tan\alpha)EI} \end{cases}. \tag{10}$$

Solving the governing equation of the beam (eqn (8)), with the boundary conditions (eqn (9)) and the solved M_0 and β_0, the deflection of the transverse beam ($w_T(x)$) can be obtained as:

$$\varphi_T(x) = \frac{F}{4EI}\left[x^2 - \frac{l(2+\tan\alpha)\tan\alpha}{2(1+\tan\alpha)}x\right]. \tag{11}$$

The overall compressive strain (λ) of the unit cell is defined as the total vertical displacement normalized by the original height (l). It comprises two parts: the displacement due to the bending of the transverse beams $\left(\frac{2w_T(0)}{l}\right)$ and the displacement due to the shear deformation of the beams. The final expression of the overall compressive strain (see Appendix A.2 for detailed derivation) is obtained as:

$$\lambda = 1 - \frac{2\omega_T}{l} - \frac{F\tan\alpha}{4\kappa GA} = 1 - \left(\frac{Fl^2\tan^3\alpha(4+\tan\alpha)}{96EI(1+\tan\alpha)}\right) - \frac{F\tan\alpha}{2\kappa GA}. \tag{12}$$

Substituting these strain expressions into eqn (6) gives the local deformation functions for the transverse and vertical beams (see Appendix A.3 for detailed derivation):

$$\begin{cases} \delta_T = 1 + \frac{Fz}{EI}\left(\frac{l\tan\alpha(2+\tan\alpha) + 4x(\tan\alpha+1)}{8(1+\tan\alpha)}\right) + \frac{1}{2\xi}\left(\frac{F}{2\kappa GA}\right)^2 \\ \delta_V = 1 + \frac{F}{EA} + \frac{Fl\tan^2\alpha(x+y)}{8(1+\tan\alpha)EI} \end{cases}, \tag{13}$$

Integrating the resistivity model (eqn (7)) over the beam volume using $R = \int_l \left[\frac{1}{\iint_A \rho^{-1}\mathrm{d}A}\right]\mathrm{d}l$, the resistance of the transverse and vertical beams can be obtained as:

$$\begin{cases} R_\mathrm{B} = \dfrac{\rho_0 l}{t^2} \\ R_\text{beam-1} = R_\text{beam-2} = \dfrac{\rho_0 \mathrm{e}^{2Xnp^{-c}\phi_\mathrm{c}^{-\frac{1}{3}}} l}{t^2} \dfrac{4EI\mathrm{e}^{\frac{Xnp^{-c}\phi_\mathrm{c}^{-\frac{1}{3}}}{\xi}\left(\frac{F}{2\kappa GA}\right)^2}}{Xnp^{-c}\phi_\mathrm{c}^{-\frac{1}{3}}Flt} \begin{pmatrix} \mathrm{dilog}\left(\mathrm{e}^{\frac{Xnp^{-c}\phi_\mathrm{c}^{-\frac{1}{3}}Flt\tan^2\alpha}{4EI(1+\tan\alpha)}}\right) - \\ 4\mathrm{dilog}\left(\mathrm{e}^{\frac{Xnp^{-c}\phi_\mathrm{c}^{-\frac{1}{3}}Flt\tan^2\alpha}{8EI(1+\tan\alpha)}}\right) + \\ 4\mathrm{dilog}\left(\mathrm{e}^{\frac{Xnp^{-c}\phi_\mathrm{c}^{-\frac{1}{3}}Flt\tan\alpha(2+\tan\alpha)}{8EI(1+\tan\alpha)}}\right) - \\ \mathrm{dilog}\left(\mathrm{e}^{\frac{Xnp^{-c}\phi_c^{-\frac{1}{3}}Flt\tan\alpha(2+\tan\alpha)}{4EI(1+\tan\alpha)}}\right) \end{pmatrix}. \\ R_\text{beam-3} = \dfrac{\rho_0 p^{-c}\mathrm{e}^{2Xnp^{-c}\phi_\mathrm{c}^{-\frac{1}{3}}} l}{t^2} \dfrac{\mathrm{e}^{-\frac{2Xnp^{-c}\phi_c^{-\frac{1}{3}}F}{EA}}\left[\dfrac{Xnp^{-c}\phi_\mathrm{c}^{-\frac{1}{3}}Fl\tan^2\alpha t}{4(1+\tan\alpha)EI}\right]^2}{2\cosh\left(\dfrac{Xnp^{-c}\phi_\mathrm{c}^{-\frac{1}{3}}Fl\tan^2\alpha t}{4(1+\tan\alpha)EI}\right) - 2} \end{cases} \tag{14}$$

In the mechanical modeling of PPN, the electrical resistance of such materials is postulated to be directly proportional to the effective electrical resistance of the GA (generalized array) units comprising the lattice structure. The relationship between the resistance (R) of PPN and the reference resistance (R_c) of the GA units can be expressed as:

$$R/R_0 = R_\mathrm{c}/R_{\mathrm{c}_0}, \tag{15}$$

where R_0 and R_{c_0} represent the initial resistance of the PPN and the GA units, respectively.

By substituting eqn (13) into eqn (2) and subsequently incorporating it into eqn (14), one can elucidate the static compressive deformation-induced pressure resistance features of porous materials.

2.4. Time-dependent piezoresistive model for PPN

In polymer materials, the inherent dynamics of polymer chains and their propensity for slippage during deformation result in distinct phenomena, such as creep hysteresis. When flexible porous resistive materials are fabricated using polymer matrices, the presence of porous structures amplifies their resistive characteristics, thereby exhibiting prominent pressure resistance attributes. Hence, the time-dependent piezoresistive properties of PPNs are primarily governed by two factors: the relaxation behavior of the polymer matrix and the structural relaxation behavior of cell ligaments. Within the polymer matrix, as shown in Fig. 4, three distinct types of molecular changes had an impact on the relaxation behavior of PPNs: alteration in bond lengths and bond angles, segmental motion, and relative slippage between molecular chains.[44] As shown in Fig. 4a, a commonly employed three-element model is utilized to characterize the relaxation properties of the material. In this model, the spring (E_1) represents the changes in bond lengths and bond angles, while the spring (E_2) and the dashpot (η_1) reflect the segmental motion and intermolecular internal friction. The governing equation for this three-element model can be written as follows:

$$\varepsilon = \frac{\sigma(t)}{E_1} + \int_0^t \sigma(t)K(t-\tau)\mathrm{d}\tau, \tag{16}$$

where $K(t-\tau) = \dfrac{\mathrm{e}^{-\frac{(t-\tau)E_2}{\eta_1}}}{\eta_1}$ is the relaxation kernel that represents the influence of the stress acting at time τ on the deformation at time t. As shown in Fig. 4b, the Kelvin–Voigt model[43–45] describes the time-dependent recovery of the bent cell ligament's shape after the external compressive load is removed. Its components are linked to the structural features. Spring E' represents the elastic restoring force driving the bent ligament back to its original straight configuration. It corresponds to the bending stiffness of the ligament. Dashpot η' models the resistance to this shape recovery, which physically originates from the relative slippage and frictional dissipation between entangled macromolecular chains during the unbending process (Fig. 4b). A Kelvin–Voigt model[51] was used to describe the creep-recovery behaviors

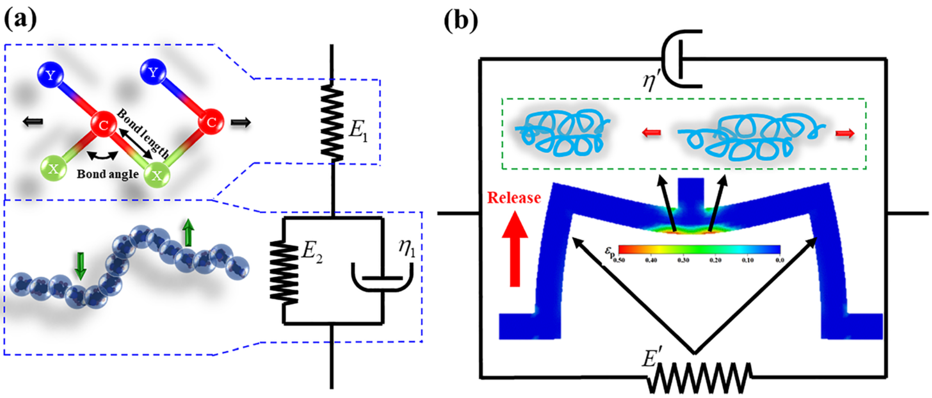

Fig. 4 Viscoelastic model of PPNs. (a) Schematic of a three-element model describing the material relaxation properties, considering the changes of polymer chain structure and bending pore wall. (b) Reasonable Kelvin viscoelastic model of the structural creep characteristics, considering the plastic strain (ε_p) of the relative slippage between the macromolecular chains as a spot (η') and the resilience of the vertical cell ligament as a spring (E').

of shear deformation as:

$$\gamma = \gamma_0\left(1 - \mathrm{e}^{-\frac{E'}{\eta'}t}\right). \tag{17}$$

Then, the time-dependent piezoresistive performance of PPNs can be represented using the following equations:

$$\begin{cases} \lambda = 1 - \left(\dfrac{l^2\tan^3\alpha(4+\tan\alpha)}{96EI(1+\tan\alpha)}\right)P(t) - \dfrac{\tan\alpha}{2\kappa GA}\Gamma(t) \\ \dfrac{R_{\mathrm{beamT}}}{R_{\mathrm{B}}} = \dfrac{4EI}{Xnp^{-c}\phi_{\mathrm{c}}^{-\frac{1}{3}}ltP(t)}\mathrm{e}^{\frac{Xnp^{-c}\phi_{\mathrm{c}}^{-\frac{1}{3}}}{\xi}\left(\frac{\Gamma(t)}{2\kappa GA}\right)^2}\left(\begin{array}{c} \mathrm{dilog}\left(\mathrm{e}^{\frac{Xnp^{-c}\phi_{\mathrm{c}}^{-\frac{1}{3}}lt\tan^2\alpha}{4EI(1+\tan\alpha)}P(t)}\right) - \\ 4\mathrm{dilog}\left(\mathrm{e}^{\frac{Xnp^{-c}\phi_{\mathrm{c}}^{-\frac{1}{3}}lt\tan^2\alpha}{8EI(1+\tan\alpha)}P(t)}\right) + \\ 4\mathrm{dilog}\left(\mathrm{e}^{-\frac{Xnp^{-c}\phi_{\mathrm{c}}^{-\frac{1}{3}}Flt\tan\alpha(2+\tan\alpha)}{8EI(1+\tan\alpha)}P(t)}\right) - \\ \mathrm{dilog}\left(\mathrm{e}^{-\frac{Xnp^{-c}\phi_{\mathrm{c}}^{-\frac{1}{3}}lt\tan\alpha(2+\tan\alpha)}{4EI(1+\tan\alpha)}P(t)}\right) \end{array}\right) \\ \dfrac{R_{\mathrm{beamV}}}{R_{\mathrm{B}}} = \dfrac{\mathrm{e}^{-\frac{2Xnp^{-c}\phi_{\mathrm{c}}^{-\frac{1}{3}}}{EA}P(t)}\left[\dfrac{Xnp^{-c}\phi_{\mathrm{c}}^{-\frac{1}{3}}l\tan^2\alpha t}{4(1+\tan\alpha)EI}P(t)\right]^2}{2\cosh\left(\dfrac{Xnp^{-c}\phi_{\mathrm{c}}^{-\frac{1}{3}}l\tan^2\alpha t}{4(1+\tan\alpha)EI}P(t)\right) - 2} \end{cases}, \tag{18}$$

with

$$\begin{cases} P(t) = \dfrac{E}{E_1}F(t) + \displaystyle\int_0^t \dfrac{E}{\eta_1}F(t)\mathrm{e}^{-\frac{(t-\tau)E_2}{\eta_1}}\mathrm{d}\tau \\ \Gamma(t) = \dfrac{E}{E_1}F(t) + \displaystyle\int_0^t \dfrac{E}{\eta_1}F(t)\mathrm{e}^{-\frac{(t-\tau)E_2}{\eta_1}}\mathrm{d}\tau + H(t-t_0)F(t_0)\left(1-\mathrm{e}^{-\frac{E'}{\eta'}t}\right), \\ H(t_0-t) = \begin{cases} 0, & (t \geq t_{0^+}) \\ 1, & (t \leq t_{0^-}) \end{cases} \end{cases} \tag{19}$$

where t_0 is the time of releasing the compression, and $E = \dfrac{E_1E_2}{(E_1+E_2)}$ is the static modulus of the three-element model. The time-dependent force ($F(t)$) in the ligaments, solved from the constitutive equations of the combined viscoelastic models (eqn (15) and (16)), governs the evolution of normal strain ($\varepsilon(t)$) and shear strain ($\gamma(t)$). These time-varying strains are then substituted into the core piezoresistive model (eqn (6) and subsequently eqn (13)) to predict the time-dependent relative resistance $\left(\dfrac{R(t)}{R_0}\right)$, as given by eqn (17). This framework explicitly decouples and integrates the material-level relaxation (*via* the three-element model) and the structure-level recovery (*via* the Kelvin model) to fully describe the observed piezoresistive creep and rebound phenomena. By substituting eqn (17), which represents the time-dependent compressive deformation of a beam, into eqn (2), which characterizes the structural relationship of the beam within a GA unit cell, one can derive the piezoresistive response characteristics of the GA unit. Furthermore, by incorporating eqn (2) into the equation that captures the relationship between the overall deformation and local deformation of porous materials, the intrinsic time-dependent piezoresistive response characteristics of porous materials can be obtained.

3. Results and discussion

3.1. Material characteristics of PPN

The materials employed in this study were fabricated using the sacrificial NaCl templating method, as depicted schematically in Fig. S1. To determine the characteristics of the CB/TPU PPNs, scanning electron microscopy (SEM) images were obtained and analyzed. By employing advanced image recognition technology, we quantified the distribution of pore diameters and pore length-width ratio, as demonstrated in Fig. 5a and b, respectively. The distribution characteristics of the pore structure are generally similar to those of previous research.[52] Typically, the pore features are centered around the size characteristics of the pore-forming agent (~25 μm) and exhibit a dispersed distribution towards both sides. This implies that the size and shape of the pores vary within a specific range and tend to concentrate near the diameter of the pore-forming agent. The supporting effect of inorganic pore-forming agents plays a crucial role in the formation and distribution of pore characteristics. Inorganic pore-forming agents provide a stable framework that helps maintain the pore structure. Therefore, under the support of inorganic pore-forming agents, the pore characteristics often maintain a circular distribution pattern. Thus, the process is controllable. To obtain precise measurements of the bulk resistance, $10 \times 10 \times 1\ \text{mm}^3$ specimens were meticulously fabricated and subjected to analysis using the four-wire method. This experimental technique (Fig. S3) was employed to eliminate the effects of contact resistances and accurately quantify the intrinsic bulk resistance of the materials under investigation. Fig. 5c and d show the resistivity curves along with different CB contents and different relative densities. Numerous studies have extensively investigated the impact of variations in conductive nanoparticles and porosity on electrical resistivity.[21] From a physical standpoint, the reduction in conductive particles and increase in porosity both lead to a decrease in the conductivity network. The phenomenon of resistance variation has been described by the percolation theory and tunneling theory, which establish an exponential relationship between electrical resistivity and the content of conductive material, as well as porosity. However, further advancements in this research involve considering factors such as microvoids generated during the material formation process,

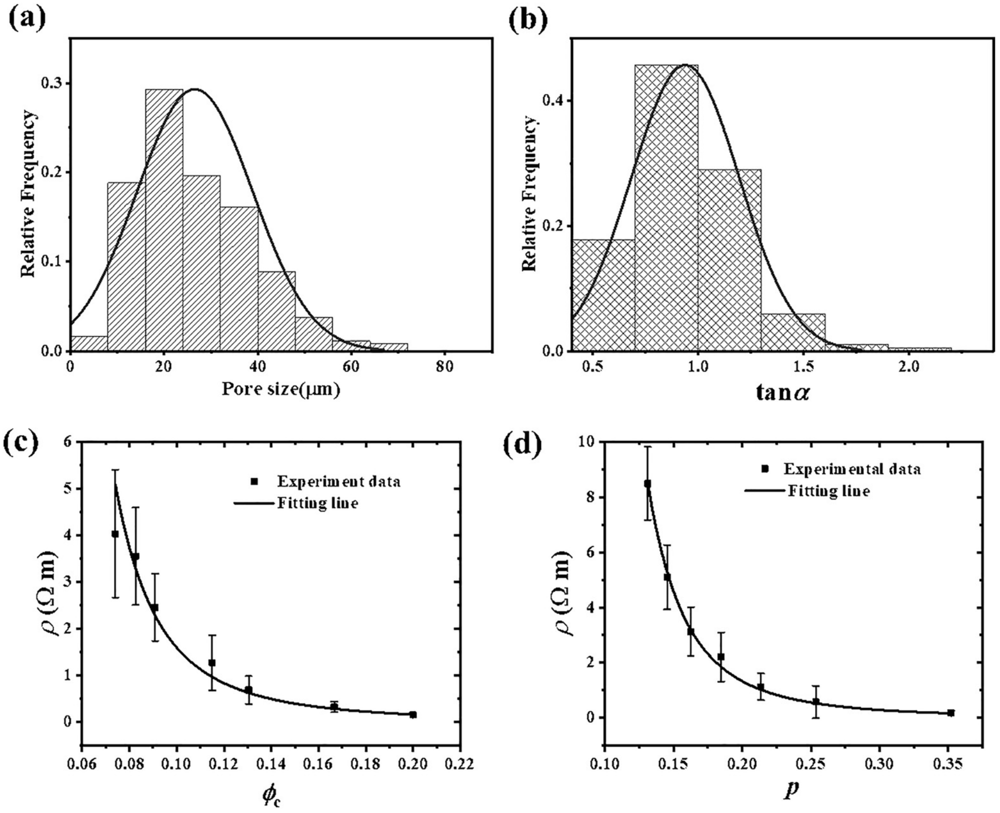

Fig. 5 Microstructure characteristics and electrical properties of PPN. Distribution of the pore diameters (a) and pore length-width ratio (b). Curves of resistivity depending on the content of CB (p = 0.224) (c) and relative density (ϕ_c = 10 v%) (d).

enabling a more accurate characterization of the relationship between electrical resistivity and variations in the content of conductive material and porosity. Based on eqn (7), the resistivity curves are well fitted ($R^2 \geq 97\%$) with free parameters $2Xn = 2.425$ and $c = 0.345$.

3.2. Piezoresistive characteristics of PPN

In this section, we investigate the intricate piezoresistive mechanism of PPNs based on the Timoshenko beam theory. The current model and experimental validation were established under constant temperature and humidity quasi-static conditions. To measure the intrinsic piezoresistive behavior, 50% compression deformation was applied to the specimens while being attached to a four-wire flexible printed circuit (FPC), as illustrated in Fig. S3. The resulting piezoresistive curves for various PPNs with different carbon black (CB) contents and relative densities are depicted in Fig. 6a and b. The analysis of the provided diagram revealed that the resistive characteristics exhibited bidirectionality, manifesting both positive and negative variations. Extensive research has been conducted on diverse porous resistive materials, with a predominant focus on investigating the positive resistive effect.[31,53–57] This line of inquiry has yielded the development of numerous highly sensitive and flexible porous resistive materials, achieving reported sensitivities of up to approximately GF ∼ 2.63.[32] Furthermore, specific investigations have explored materials demonstrating a negative resistive effect,[58–60] such as CNT/TPU foam, attributing this phenomenon to carbon nanotube fracture.[59,60] However, it is noteworthy that many foam composites employing CNT as the conductive material have been proposed, consistently exhibiting positive resistive effects.[57,59,61] The present study elucidates the bidirectional resistive characteristics of composite materials from mechanical deformation. At low porosity levels, characterized by thick pore walls, compression readily induced the shear deformation of the pore walls, resulting in an increase in resistance. Conversely, at high porosity levels, compression primarily induced the bending of the pores, leading to a decrease in resistance. Substituting the free parameters ($2Xn = 2.425$ and $c = 0.345$) into eqn (13), (2) and (11), the fitting curve of the piezoresistive curves, based on the ADAM algorithm (S3), was obtained and showed good agreement with experimental results (Fig. S4 and S6). As shown in Fig. 6a, the PPN, with a low CB content ($\phi_c = 5$ v%) and high relative density ($p = 0.224$), exhibits obvious negative piezoresistive behavior

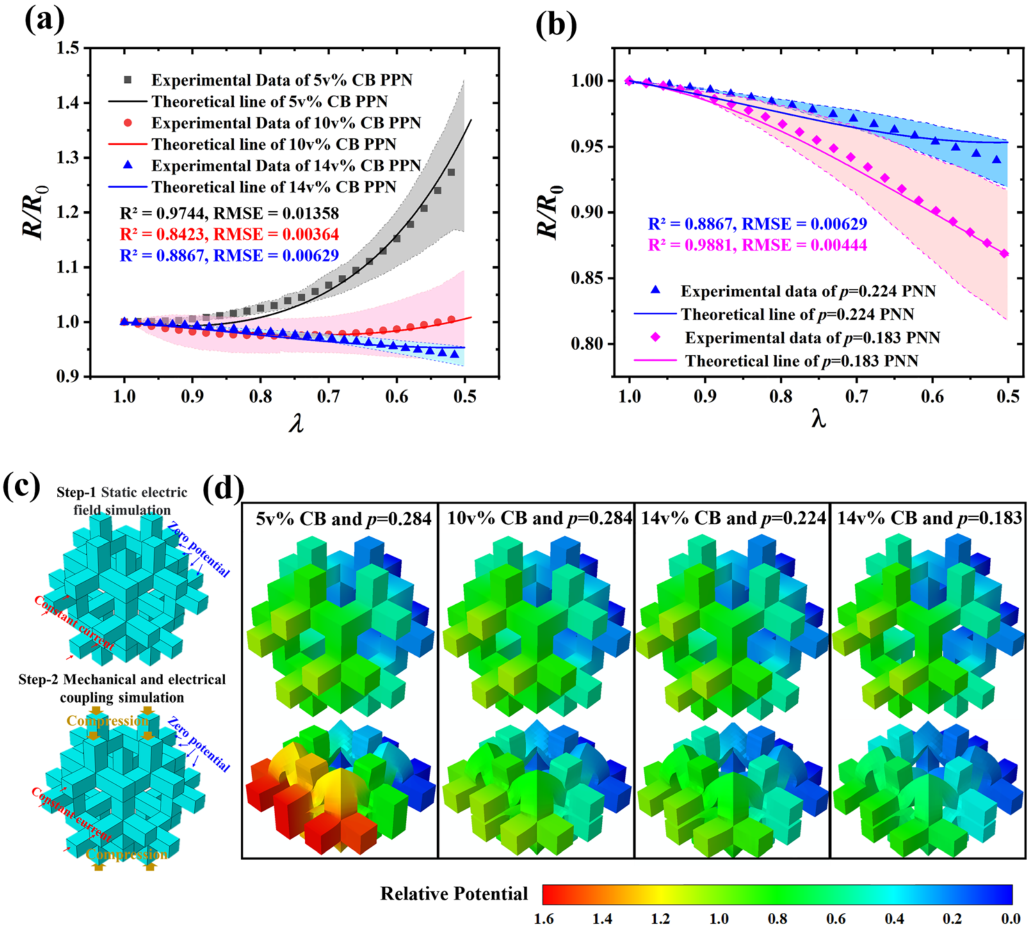

Fig. 6 Piezoresistive characteristics of PPN. Experimental and theoretical piezoresistive curves of PPN with different CB contents ($p = 0.224$) (a) and different relative densities ($\phi_c = 14$ v%) (b). (c) Schematic of two-step loading in simulation. (d) Relative resistance (R/R_0) distribution of different GA cells under compressed deformation ($\lambda = 0.55$) from the FEA model.

(resistance increases with the decrease in elongation), which can be described by the theoretical model with a constraint efficacy factor of $\xi = 0.095$. Increasing the CB content ($\phi_c = 14$ v%) will increase the constraint efficacy factor ($\xi = 0.15$) to reduce the negative piezoresistive response. As shown in Fig. 6b, decreasing the relative density ($p = 0.224$ and $p = 0.183$) increases the constraint efficacy factor ($\xi = 0.25$ and $\xi = 1$), which will result in an increase in the positive piezoresistive response. While the fitted ξ values show a systematic and physically plausible correlation with sample composition and piezoresistive sign, their direct quantitative mapping to a fundamental polymer property, such as crosslink density, requires further dedicated investigation. Here, it served as an effective phenomenological parameter within the proposed model framework. In the theoretical model based on the Timoshenko beam theory, it was assumed that the deformation in the thickness direction was uniform, which approximated the deformation characteristics of slender beams with small aspect ratios. However, to further investigate the degree of fidelity of the theoretical model to three-dimensional structures, a three-dimensional finite element simulation model was constructed. This three-dimensional finite element model considered the three-dimensional properties of materials and geometry, allowing for an accurate description of the structure's deformation and stress distribution. By comparing the results of the theoretical model with the three-dimensional finite element simulation model, the suitability and fidelity of the theoretical model to three-dimensional structures could be evaluated. The 3D geometric model of PPNs, with ideal beam frames and repetitive units, was established in the commercial FEM software ABAQUS with a UMAT subprogram (S5) to study the intrinsic piezoresistive response. Because of the similarity between thermal governing equations and electrical governing equations, static thermomechanical modules in the ABAQUS software were applied to simulate electromechanical behaviors. It mapped electrical conductivity, current, and voltage directly to thermal conductivity, heat flux, and temperature within the solver. In the FEA model, coupled temperature-displacement elements were applied to analyze the resistance-deformation relationships, and 13 000 C3D8T elements were used to disperse the model to yield convergent results (Fig. S7). The loading conditions for the 3D simulation model are shown in Fig. 6c. The compression process of the material was simulated by applying displacement conditions on the upper surface. A constant current was applied to the front surface, while the back surface was set to zero potential. By utilizing the proportional relationship between potential and resistance, the change in resistance could be analyzed through the variation in potential. Fig. 6d shows the relative resistance $\left(\frac{R}{R_0}\right)$ distribution of different GA cells under the compression deformation, ($\lambda = 0.55$), based on the FEA model. Furthermore, the accuracy of the theoretical model was validated by the FEM results, as shown in Fig. 6.

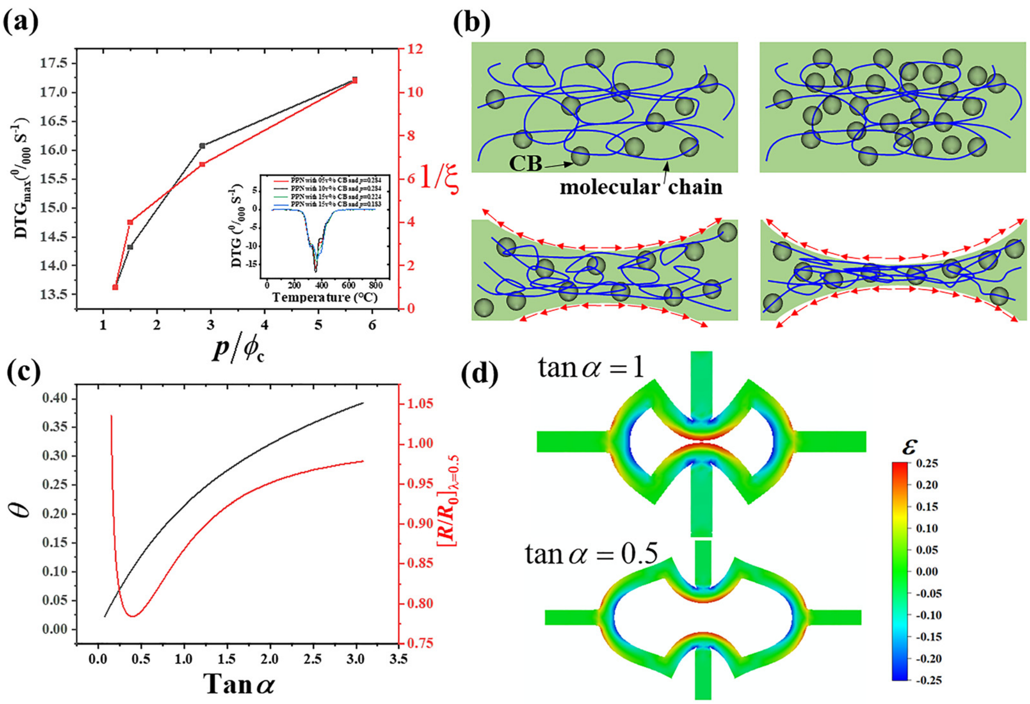

Fig. 7 Effect of key parameters (relative density (p), CB content (ϕ_c) and length-width ratio ($\tan\alpha$)) on piezoresistive behaviors. (a) Maximum derivative thermogravimetry (DTG) value (left Y-axis, in ‰/s) and inverse constraint efficacy factor $1/\xi$ (right Y-axis, dimensionless), *versus* p/ϕ_c ratio. Inset: Corresponding full DTG curves (DTG *vs.* temperature) with these different combinations of CB content and relative density. (b) Schematic of the effect of CB content and relative density on effective constraint factor. (c) Structural parameter (θ) of the cell ligament and relative resistance ($\lambda = 0.5$), changing with the length-width ratio ($\tan\alpha$) of PPN ($p = 0.184$). (d) Strain distribution of the GA cells with different tan α values ($\tan\alpha = 1$ and $\tan\alpha = 0.5$).

Fig. 7 shows the immediate effect of key parameters (p, ϕ_c and $\tan\alpha$) on the piezoresistive behaviors. The constraint efficacy factor (ξ) mainly depended on the relative density and CB content. According to the derivative thermogravimetric analysis, the derivative thermogravimetric rate (DTG) characterized the thermal stability of the polymer and the fracture energy of chemical bonds. The DTG′ $\left(\mathrm{DTG}' = \mathrm{DTG}\cdot\frac{m_{\mathrm{total}}}{(m_{\mathrm{total}} - m_{\mathrm{residual}})}\right)$ of PPNs, with different relative densities (p) and CB contents (ϕ_c), is shown in Fig. 7a. The small value of $\mathrm{DTG}'_{\max}$ and the occurrence of a weight loss at a high temperature are often indicative of a higher thermal stability, which, in the context of polymer networks, is commonly associated with a higher crosslinking density.[62] In the context of our model, a relatively high crosslinking degree directly contributed to a significantly constrained polymer network, which was phenomenologically captured by a high constraint efficacy factor (ξ). A similar mechanistic distinction underpins the comparison between CNT/PDMS foam and CNT/epoxy foam.[59,63,64] Epoxy resin, a thermosetting polymer with a highly crosslinked structure, provides a strong constraint against filler separation. In contrast, PDMS, with its relatively low crosslinking density, allows for more flexibility and chain slippage. Under compression, this leads to an increased tunneling gap in the CNT/PDMS foam (high resistance) but a reduced gap in the constrained CNT/epoxy foam (low resistance). These observations support our model's premise that the effective constraint of the matrix, which is influenced by its crosslinking degree, is a key determinant of the piezoresistive behavior.

The schematic presented in Fig. 7b further illustrates how material composition and structure govern this effective constraint. Increasing the carbon black (CB) content enhanced interfacial interactions (*e.g.*, hydrogen bonding), which reduced chain slippage and increased the effective constraint (ξ) (top in Fig. 7b). A similar trend of improved constraint with high filler content was observed in systems such as graphene/TPU foam and functionalized graphene/LLDPE composites.[65–68] Moreover, reducing the relative density (increasing porosity) decreased ligament thickness. This increased interfacial tension, thereby promoting greater chain entanglement and, consequently, a higher effective degree of constraint against slippage.

In thermogravimetric analysis, while a porous structure might theoretically accelerate heat transfer and weight loss, both prior work[65,69,70] and our data presented in Fig. 7a show the opposite: high porosity correlates with a reduced rate of thermal weight loss. This was attributed to the significant interfacial tension at high porosity, which refined the microstructure (thin ligaments) and enhanced the material's stability and effective constraint (bottom in Fig. 7b). Therefore, thermogravimetric trends corroborated that structures with relatively high porosity exhibited significant resistance to chain slippage—a microstructural state that our model interpreted and quantified as a high fitted value of the constraint efficacy factor (ξ).

In addition to the aforementioned factors influencing the stability of polymer chains, the impact of porous structures on pressure resistance sensitivity was further illustrated. Fig. 7c shows the structural parameter (θ) of cell ligament and relative resistance (λ = 0.5), varying with respect to the length-width ratio ($\tan\alpha$) of PPNs (p = 0.184). The structural parameter (θ) increased with the increase in the length-width ratio ($\tan\alpha$) of PPNs. The minimum relative resistance (λ = 0.5), which means maximum sensitivity, occurred at $\tan\alpha$ = 0.5. Two different strain contours, as shown in Fig. 7d, depicting different structural configurations and obtained from finite element simulation analysis models, could provide a more intuitive representation of the influence of porous structures on piezoresistive characteristics. The strain contour showed that reducing the length-width ratio ($\tan\alpha$) could reduce the maximum principal strain (ε) to reduce the resistance.

3.3. Time-dependent piezoresistive characteristics for PPN

Porous resistive sensors exhibit excellent characteristics, such as high compressibility, high pressure sensitivity, and high resilience.[71] However, during the investigation of their transient response characteristics, many studies have observed that the resistance rebound after rapid release is higher than the initial resistance.[72] Previous research attributed this phenomenon to reasons such as crack propagation and the release of internal elastic potential energy, which do not align well with the recoverability of the rebound resistance and the stress–strain hysteresis loop.[32,59] Our analytical model in this section revealed that during the compression process, resistance decrease (caused by the compressed region due to beam bending) and resistance increase (caused by the stretched region due to beam deformation) occurred simultaneously. Furthermore, in the recovery process, the time required for molecular chain movement to recover from stretching was significantly longer than the time taken for the molecular bond changes induced by compression. Based on both the Timoshenko theory and viscoelastic theory, the time-dependent piezoresistive behaviour of PPNs was analyzed. Many experimental tests were carried out to fit the theoretical results to obtain the relaxation time of resistance. Fig. 8a shows the experimental and theoretical piezoresistive curves $\left(\frac{E_2}{(E_1+E_2)} = 0.8,\ \frac{\eta_1}{E_2} = 10\ \mathrm{s},\ \text{and}\ \frac{\eta'}{E'} = 200\ \mathrm{s}\right)$ including compression, relaxation, and creep of resistance. The good agreement between the experimental results and theoretical results demonstrated the accuracy of the theoretical model. Furthermore, the rebounding resistance increased with the compression deformation due to the increase in slow-recovery shear strain. Based on the Flory–Haggin model and the experimental results, the assumption that normal strain was mainly generated from the configurational change of molecular chains was approved, while the shear strain resulted in segmental slippage and movement.[44,48,49] Therefore, Fig. 8b shows the time-dependent piezoresistive curves of different PPNs (with ξ = 0.25 and ξ = 1). More obvious rebounding resistance of the PPNs with p = 0.224, ϕ_c = 14 v% and was a further proof of the

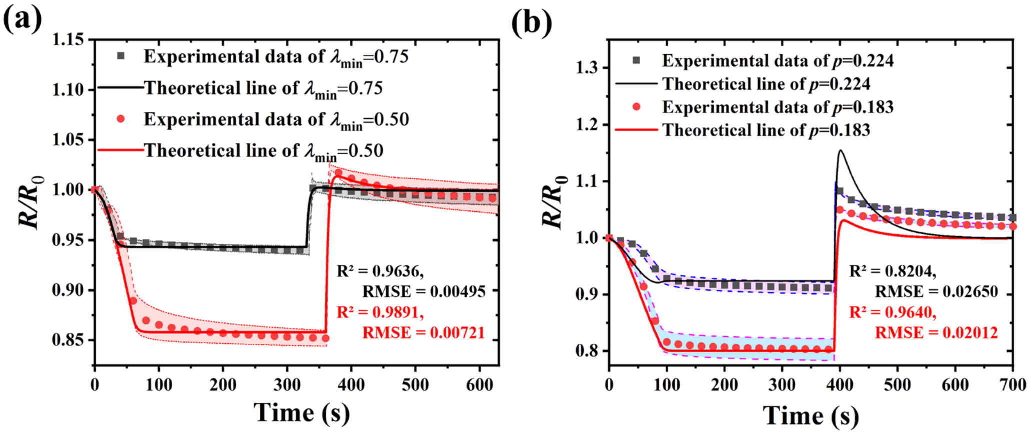

Fig. 8 Time-dependent behaviors of CB/TPU PPN. (a) Experimental results and analytical results of PPN (ξ = 1, ϕ_c = 14 v%, p = 0.183) under different loadings. (b) Experimental results and analytical results of PPN (ξ = 0.25, ϕ_c = 14 v%, p = 0.224) and PPN (ξ = 1, ϕ_c = 14 v%, p = 0.183).

assumption. Finally, the above results demonstrate the accuracy of the theoretical results and explain the unique creep behavior of the resistance of PPNs.

4. Conclusion

This study presents a theoretical model that elucidates the intrinsic piezoresistive mechanism of conductive porous nanocomposites (PPNs) under small-to-moderate compressive strains. By directly coupling the micromechanics of ligament bending—modeled *via* the Timoshenko beam theory—with the evolution of the conductive network governed by quantum tunneling, the model successfully predicts the electromechanical response of carbon black/thermoplastic polyurethane (CB/TPU) PPNs across a range of compositions and relative densities. Excellent agreement between the theoretical predictions and experimental data ($R^2 > 0.97$) validates the model's accuracy. Under small-to-moderate compressive strains (<50%), the bending of cell ligaments, rather than pore closure, is the dominant deformation mode governing the piezoresistive response. The model quantitatively links this mechanism to key microstructural parameters, revealing that the positive piezoresistive sensitivity (*i.e.*, resistance decrease upon compression) increases with higher porosity, greater constraint efficacy factor, and larger pore height-to-width ratios. Furthermore, by incorporating viscoelasticity (Kelvin–Voigt model), the framework accurately captures the time-dependent relaxation and creep-recovery behaviors of PPNs, attributing the observed resistance rebound to the slower recovery of polymer chain segmental motion compared to configurational changes. This work transcends phenomenological fitting, providing a physics-guided, microstructure-informed toolset for the rational design of high-performance PPN sensors. The current analysis is limited to linear deformations under small-to-moderate compressive strains, and nonlinear behavior under large strains remains a subject for future investigation. Overall, this study underscores the critical role of rational micro/nano-structural design in unlocking the full potential of PPNs for advanced flexible sensing applications.

Conflicts of interest

The authors declare that they have no known competing financial interests or personal relationships that could have appeared to influence the work reported in this paper.

Data availability

The original datasets are available from the corresponding author upon reasonable request.

Supplementary information includes experimental details on sample fabrication and characterization, additional fitting algorithms (ADAM optimization), finite element analysis procedures, and detailed mathematical derivations of the theoretical model. See DOI: https://doi.org/10.1039/d5tc03384e.

Acknowledgements

This work was financially supported by the Science, Technology and Innovation Commission of Shenzhen Municipality under grant KQTD20170810105439418 and the National Natural Science Foundation of China (62371298).

References

1 N. Parvin, V. Kumar, T. K. Mandal and S. W. Joo, *J. Funct. Biomater.*, 2024, **15**, 226.
2 Y. Jung, Y. Huh and D. Kim, *Microporous Mesoporous Mater.*, 2021, **310**, 110673.
3 M. Yang, Z. Ye, Y. Ren, M. Farhat and P.-Y. Chen, *Micromachines*, 2023, **14**, 603.
4 Y. He, L. Zhao, J. Zhang, L. Liu, H. Liu and L. Liu, *Compos. Sci. Technol.*, 2020, **200**, 108419.
5 A. Vasanth, A. Ashok, T. N. Do and H.-P. Phan, *Adv. Colloid Interface Sci.*, 2025, 103439.
6 S. Zhao and R. Zhu, *Adv. Mater. Technol.*, 2019, **4**, 1900414.
7 H. Tetik, Y. Wang, X. Sun, D. Cao, N. Shah, H. Zhu, F. Qian and D. Lin, *Adv. Funct. Mater.*, 2021, **31**, 2103410.

8 B. Hao, L. Mu, Q. Ma, S. Yang and P.-C. Ma, *Compos. Sci. Technol.*, 2018, **163**, 162–170.
9 H. Chen, L. Miao, Z. Su, Y. Song, M. Han, X. Chen, X. Cheng, D. Chen and H. Zhang, *Nano Energy*, 2017, **40**, 65–72.
10 Y.-F. Fu, F.-L. Yi, J.-R. Liu, Y.-Q. Li, Z.-Y. Wang, G. Yang, P. Huang, N. Hu and S.-Y. Fu, *Compos. Sci. Technol.*, 2020, **186**, 107910.
11 M. Eskandari-Ghadi and Y. Zhang, *Int. J. Solids Struct.*, 2022, **242**, 111533.
12 P. S. Liu and X. M. Ma, *Mater. Des.*, 2020, **188**, 108413.
13 I. J. Gibson and M. F. Ashby, *Proc. R. Soc. London, Ser. A*, 1982, **382**, 43–59.
14 Y. Songlin, H. Chai, Y. Xiong, M. Kang, C. Geng, Y. Liu, Y. Chen, Y. Zhang, Q. Zhang, C. Li, H. Wei, Y. Zhao, F. Yu and A. Lu, *Adv. Mater.*, 2022, **34**, 2200908.
15 M. Zhang, D. Yan, J. Wang and L.-H. Shao, *J. Mech. Phys. Solids*, 2021, **151**, 104396.
16 L. Gong, S. Kyriakides and N. Triantafyllidis, *J. Mech. Phys. Solids*, 2005, **53**, 771–794.
17 S. Babaee, B. H. Jahromi, A. Ajdari, H. Nayeb-Hashemi and A. Vaziri, *Acta Mater.*, 2012, **60**, 2873–2885.
18 C. Betts, *Mater. Sci. Technol.*, 2012, **28**, 129–143.
19 X. Zhang, Y. Wu, L. Tang, Z. Liu, Z. Jiang, Y. Liu and H. Xi, *Mech. Adv. Mater. Struct.*, 2018, **25**, 1265–1275.
20 M. Sans, O. Farges, V. Schick and G. Parent, *Int. J. Therm. Sci.*, 2022, **179**, 107656.
21 H. Liu and X. Zhao, *Int. J. Heat Mass Transfer*, 2022, **183**, 122089.
22 W. He, X. Peng, F. Xin and T. J. Lu, *Compos. Sci. Technol.*, 2022, **227**, 109607.
23 Y. Liao, Z. Wang, X. Sun, W. Lou, H. Liu and B. Sun, *Chem. Eng. J.*, 2022, **433**, 133830.
24 L. Sarkisov, *Adv. Mater.*, 2012, **24**, 3130–3133.
25 J. Tian, C. Qi, Y. Sun, Z. M. Yaseen and B. T. Pham, *Eng. Comput.*, 2021, **37**, 3455–3471.
26 B. Zhao, M. Hamidinejad, S. Wang, P. Bai, R. Che, R. Zhang and C. B. Park, *J. Mater. Chem. A*, 2021, **9**, 8896–8949.
27 H. Ji, S. Zhang, K. Liu, T. Wu, M. Xu and S. Shen, *J. Phys. D: Appl. Phys.*, 2020, **53**, 125302.
28 S. Zhang, X. Liang, M. Xu, B. Feng and S. Shen, *Appl. Phys. Lett.*, 2015, **107**, 142902.
29 K. Cordero-Edwards, H. Kianirad, C. Canalias, J. Sort and G. Catalan, *Phys. Rev. Lett.*, 2019, **122**, 135502.
30 D. D. L. Chung, *J. Mater. Sci.*, 2020, **55**, 15367–15396.
31 X. Shi, Y. Zhu, X. Fan, H.-A. Wu, P. Wu, X. Ji, Y. Chen and J. Liang, *Matter*, 2022, **5**, 1547–1562.
32 Y. Li, S. Luo, M.-C. Yang, R. Liang and C. Zeng, *Adv. Funct. Mater.*, 2016, **26**, 2900–2908.
33 T. Han, H. Yan, D. Xu and L.-Y. Fu, *Earth-Sci. Rev.*, 2020, **211**, 103420.
34 A. S. Fiorillo, C. D. Critello and S. A. Pullano, *Sens. Actuators, A*, 2018, **281**, 156–175.
35 H. Yang, L. Yuan, X. Yao and D. Fang, *J. Mech. Phys. Solids*, 2020, **139**, 103943.
36 Y. Qin, M. Qu, Y. Pan, C. Zhang and D. W. Schubert, *Composites, Part A*, 2020, **129**, 105724.
37 J. Zhang, Z. Wang and Z. Peng, *Adv. Theory Simul.*, 2021, **4**, 2100247.
38 R. Patel, M. Lu, S. H. Diermann, A. Wu, A. Pettit and H. Huang, *J. Mech. Behav. Biomed. Mater.*, 2019, **96**, 1–8.
39 X. Liu, G. Su, Q. Guo, C. Lu, T. Zhou, C. Zhou and X. Zhang, *Adv. Funct. Mater.*, 2018, **28**, 1706658.
40 T. A. Ezquerra, M. Kulescza, C. S. Cruz and F. J. Baltá-Calleja, *Adv. Mater.*, 1990, **2**, 597–600.
41 T. Chen, G. Y. Su, Y. S. Shen, B. Gao, X. Y. Li and R. Müller, *Int. J. Mech. Sci.*, 2016, **113**, 211–220.
42 W. Li, X. Jin, X. Han, Y. Li, W. Wang, T. Lin and Z. Zhu, *ACS Appl. Mater. Interfaces*, 2021, **13**, 19211–19220.
43 W. Voigt, *Abh. K. Ges. Wiss. Goettingen*, 1890, **36**, 3–48.
44 M. Rubinstein and R. H. Colby, *Polymer physics*, Oxford University Press, New York, 2003.
45 R. M. Christensen, *Theory of viscoelasticity*, Courier Corporation, 2013.
46 J. Zhang, S. Wei, C. Liu, C. Shang, Z. He, Y. Duan and Z. Peng, *Microsyst. Nanoeng.*, 2024, **10**, 19.
47 S. Paszkiewicz, I. Taraghi, A. Szymczyk, A. Huczko, M. Kurcz, B. Przybyszewski, R. Stanik, A. Linares, T. A. Ezquerra and Z. Rosłaniec, *Compos. Sci. Technol.*, 2017, **146**, 20–25.
48 P. T. P. Aryanti, D. Ariono, A. N. Hakim and I. G. Wenten, *J. Phys.: Conf. Ser.*, 2018, **1090**, 012074.
49 M. Huo and Y. Guo, *Polymers*, 2020, **12**, 335.
50 K. F. Wang, B. L. Wang and J. E. Li, *Energy*, 2020, **191**, 116560.
51 T. Zhai, D. Li, G. Fei and H. Xia, *Composites, Part A*, 2015, **72**, 108–114.
52 D.-S. Shim, *J. Mater. Res. Technol.*, 2021, **15**, 119–134.
53 X. Li, X. Li, T. Liu, Y. Lu, C. Shang, X. Ding, J. Zhang, Y. Feng and F.-J. Xu, *ACS Appl. Mater. Interfaces*, 2021, **13**, 46848–46857.
54 Y. Lv, B. Wang, G. Liu, Y. Tang, E. Lu, K. Xie, C. Lan, J. Liu, Z. Qin and L. Wang, *Front. Bioeng. Biotechnol.*, 2021, **9**, 641130.
55 C. Schlumberger and M. Thommes, *Adv. Mater. Interfaces*, 2021, **8**, 2002181.
56 Z. Tang, S. Jia, C. Zhou and B. Li, *ACS Appl. Mater. Interfaces*, 2020, **12**, 28669–28680.
57 Z. Wang and X. Ye, *Nanotechnology*, 2014, **25**, 285502.
58 S. Biccai, C. S. Boland, D. P. O'Driscoll, A. Harvey, C. Gabbett, D. R. O'Suilleabhain, A. J. Griffin, Z. Li, R. J. Young and J. N. Coleman, *ACS Nano*, 2019, **13**, 6845–6855.
59 Q. Ma, B. Hao, X. Yue and P.-C. Ma, *Polymer*, 2022, **257**, 125288.
60 F. Avilés, A. I. Oliva-Avilés and M. Cen-Puc, *Adv. Eng. Mater.*, 2018, **20**, 1701159.
61 Y. Wang, S. Wang, M. Li, Y. Gu and Z. Zhang, *Sens. Actuators, A*, 2018, **273**, 140–146.
62 N. M. Kanafi, N. A. Rahman and N. H. Rosdi, *Mater. Today: Proc.*, 2019, **7**, 721–731.
63 D. Lu, Z. Mo, B. Liang, L. Yang, Z. He, H. Zhu, Z. Tang and X. Gui, *Carbon*, 2018, **133**, 457–463.
64 W. A. Laftah, W. A. W. A. Rahman and A. N. Ibrahim, *RSC Adv.*, 2025, **15**, 14838–14847.

65 C. Feng, Z. Yi, X. Jin, S. M. Seraji, Y. Dong, L. Kong and N. Salim, *Composites, Part B*, 2020, **194**, 108065.

66 H. Liu, M. Dong, W. Huang, J. Gao, K. Dai, J. Guo, G. Zheng, C. Liu, C. Shen and Z. Guo, *J. Mater. Chem. C*, 2017, **5**, 73–83.

67 N. H. Kim, T. Kuila and J. H. Lee, *J. Mater. Chem. A*, 2013, **1**, 1349–1358.

68 N. H. Kim, T. Kuila and J. H. Lee, *J. Mater. Chem. A*, 2014, **2**, 2681–2689.

69 K. Lafdi, O. Mesalhy and S. Shaikh, *J. Appl. Phys.*, 2007, **102**, 083549.

70 R. Coble and W. Kingery, *J. Am. Ceram. Soc.*, 1955, **38**, 33–37.

71 C. Huang, Z. Bian, C. Fang, X. Zhou and J. Song, *J. Appl. Mech.*, 2018, **85**, 041009.

72 H. Liu, M. Dong, W. Huang, J. Gao, K. Dai, J. Guo, G. Zheng, C. Liu, C. Shen and Z. Guo, *J. Mater. Chem. C*, 2017, **5**, 73–83.